Modeling the droplet break-up based on drawing the shape using velocity gradient and normal vector

S.Heydarpoor, Tarbiat Modares University, Tehran, Iran

Prof. M.H.N.Famili*, PHD, Tarbiat Modares University, Tehran, Iran

nfamili@modares.ac.ir

Abstract

The present study developed a model to deform a viscous droplet in a viscous matrix by a shear flow based on changing the normal vector. The initial cross-section was assumed to be a regular polygon with 1000 sides instead of a circle or ellipsoid, and also this model was independent of the initial polygon shape. Changing the normal vector and the length of each side of the droplet was a function of the velocity gradient. To calculate the velocity gradient over each side of the shape, the equations of tangential and normal stress, the conservation of mass equation, and the absence of mass transfer equation between two phases were solved simultaneously. By knowing the velocity gradient, normal vectors and the length of each side are calculated; therefore, the new shape can be plotted by drawing sides one after another. The results displayed that the time of the break-up, which this model predicts, coincides with the experimental results. On the other hand, the predicted shape of the droplet at the break-up has logically coincided with the experimental results in the middle range of the Capillary number ratio (1.4 -2.6 critical Capillary number). The drop's dimensions show less than 30% deviation and its rotation less than 20%. Additionally, the dimension of the end bubble also shows a deviation of less than 40%.

Keywords: Break-up, viscous droplet, shear flow, velocity gradient, normal vector.

1-Introduction

One of the challenging issues in investigating high viscous emulsions is the deformation and break-up of a viscous droplet in a viscous matrix. Therefore, different study methods have been developed to overcome such challenges.

Analytical methods explore the initial regular shape of droplets, i.e., sphere and ellipsoid. At the same time, the experimental results display the deformation of the droplet to an irregular shape and its following break-

up. Moreover, most of the analytical methods had been extended based on the average of parameters on the droplet surface[1-4]. Some others had been structured by capillary number, viscosity ratio, and volume fraction of droplets[5-10]. Numerical models encompass the volume of the fluid scheme and the average of viscosity and density as parameters for the Navier-Stokes equation to solve it numerically[11]. The other study examined the alteration of a droplet's shape and its break up in turbulent flow. A level set and volume of fluid method was employed to investigate two-phase cross flow. Additionally, the study evaluated the impact of nozzle geometry on the trajectory and breakup of the spray[12].

One of the most crucial areas of research in two-phase materials is the utilization of velocity gradient to analyze droplets by means of stream function. This method involves studying how the droplet shape changes with respect to the shear rate of the matrix. In this model, the droplet's shape is plotted as a function of time to better understand its behavior[13].

The present model represents the deformation and break up of a single droplet with μ_d viscosity in a matrix with μ_m viscosity, constant interfacial tension coefficient, and a low Reynolds number. The gravity effect is also neglected. It is assumed that the initial shape of the cross-section of the droplet is a regular polygon instead of a circle. At the same time, each side has a unique normal vector perpendicular to its beginning. The matrix shear flow field evolves the normal vector of each point at the surface of droplet. In other words, every point at each time has a unique normal vector that will be deformed at a later time by the function of the velocity gradient. On the other hand, the length of all sides also would be changed under shear flow as a function of the velocity gradient. The advantage of this model compared to other previous methods is that there is no meshing in this method and in each time step a new shape is drawn based on the shape in the previous time.

2-Model development

The initial shape of droplet is considered to be a disc with 1000 sides in a two-dimension polygon cross-section with a fixed thickness of 1 that could be deformed (Fig.1). Therefore, the normal vectors at all points

over the droplet and the length of all sides (lateral area of each side) are precisely defined. Eq. (1) displays the deformation rate of normal vector by velocity gradient tensor. Eq. (2) also verifies the rate of the change of the length of any side (lateral area of each side) by the velocity gradient[14].

$$\frac{d(\bar{n}_i)}{dt} = (\bar{n}_i . \bar{\bar{L}}_i . \bar{n}_i)\bar{n}_i - \bar{\bar{L}}^T{}_i . \bar{n}_i \rightarrow n_i^t = \bar{n}_i^{t-1} + \Delta t((\bar{n}_i^{t-1} . \bar{\bar{L}}_i^{t-1} . \bar{n}_i^{t-1})\bar{n}_i^{t-1} - \bar{\bar{L}}^T{}_i^{t-1} . \bar{n}_i^{t-1}) \quad (1)$$

$$\frac{d(S_i)}{dt} = (tr\,\bar{\bar{L}}_i - \bar{n}_i . \bar{\bar{L}}_i . \bar{n}_i)S_i \rightarrow S_i^t = S_i^{t-1} + \Delta t((tr\,\bar{\bar{L}}_i^{t-1} - \bar{n}_i^{t-1} . \bar{\bar{L}}_i^{t-1} . \bar{n}_i^{t-1})S_i^{t-1}) \quad (2)$$

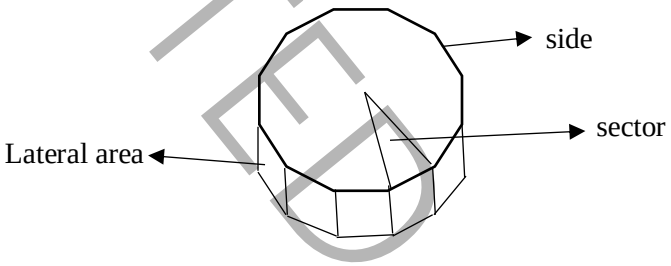

Fig. 1. Scheme of initial shape of droplet

By reducing the time step, the solution of Eq. (1) and (2) becomes more accurate to the point where there is no significant change in the solution of these equations by reducing the time step. The calculated optimal time step is 0.1 seconds. To calculate **n** and S at any time, the solution must be done step by step from time zero to t. For example, to calculate the third second, it is necessary to take 30-time steps of 0.1 second.

The stress balance equations should be solved over and inside the side interface to determine the velocity gradient. It should be noted that in the previous study, the equation of stress balance was presented for the same viscosity of droplet and matrix over the entire droplet surface[3].

There are two types of forces, namely the interfacial force and shape relaxation force, that resist drop elongation. It is assumed that in Eq. (3) and (4) the shape relaxation of the drop is ignored and the term of dissipation of stress from bulk to the vicinity of the interface is also negligible.

Eq. (3) displays the stress of the matrix exerted over the droplet and tensor (4) shows the stress inside the droplet surface. To calculate four components of the velocity gradient tensor (**L**) of each side at the interface, four Eqs (5-8) should be solved simultaneously.

Eq (5) is the tangential part balance of the shear stress of the interface, and Eq (6) is the normal part of the mentioned shear stress. The left side of equation 6 shows the difference between the normal part of the shear stress (force) inside and outside the droplet. The right side of equation 6 shows the pressure difference caused by the shear stress, which causes the droplet to break-up. Eq (7) is relevant to the assumption of conservation of mass, whereas Eq (8) explains that the mass transfer phenomenon did not occur at the interface[15].

$$(\overline{\overline{\sigma}}_{over})_i^t = \lambda^{-1}\left|\mu_m - \mu_d\right|\begin{bmatrix} \dot{\gamma}_{mxx} & \dot{\gamma}_{mxy} \\ \dot{\gamma}_{myx} & \dot{\gamma}_{myy} \end{bmatrix} - \mu_d \begin{bmatrix} 2(\frac{\partial u}{\partial x})_i^t & (\frac{\partial u}{\partial y})_i^t + (\frac{\partial v}{\partial x})_i^t \\ (\frac{\partial u}{\partial y})_i^t + (\frac{\partial v}{\partial x})_i^t & 2(\frac{\partial v}{\partial y})_i^t \end{bmatrix} \quad (3)$$

$$(\overline{\overline{\sigma}}_{d})_i^t = \mu_d \begin{bmatrix} 2(\frac{\partial u}{\partial x})_i^t - \frac{\Gamma S_i^t}{V\mu_d}\left((n_{xi}^t)^2 - 0.5\right) & \left((\frac{\partial u}{\partial y})_i^t + (\frac{\partial v}{\partial x})_i^t\right) - \frac{\Gamma S_i^t}{V\mu_d} n_{xi}^t n_{yi}^t \\ \left((\frac{\partial u}{\partial y})_i^t + (\frac{\partial v}{\partial x})_i^t\right) - \frac{\Gamma S_i^t}{V\mu_d} n_{xi}^t n_{yi}^t & 2(\frac{\partial v}{\partial y})_i^t - \frac{\Gamma S_i^t}{V\mu_d}\left((n_{yi}^t)^2 - 0.5\right) \end{bmatrix} \quad (4)$$

$$(\sigma_{TANGETIAL})_i^t = ((\overline{\overline{\sigma}}_{over})_i^t . \overline{n}_i^t - (\overline{\overline{\sigma}}_{d})_i^t . \overline{n}_i^t) . \overline{T}_i^t = 0 \quad (5)$$

$$(\sigma_{NORMAL})_i^t = ((\overline{\overline{\sigma}}_{over})_i^t . \overline{n}_i^t - (\overline{\overline{\sigma}}_{d})_i^t . \overline{n}_i^t) . \overline{n}_i^t = -\Gamma \frac{V_i^t}{V} \kappa_i^t \left(\overline{n}_i^t . \overline{n}_i^t\right) \quad (6)$$

$$\left(\nabla . \overline{U}\right)_i^t = 0 \rightarrow (\frac{\partial u}{\partial x})_i^t + (\frac{\partial v}{\partial y})_i^t = 0 \rightarrow \left(\frac{\partial v}{\partial y}\right)_i^t = \left(-\frac{\partial u}{\partial x}\right)_i^t \quad (7)$$

$$\overline{U}_i^t . \overline{n}_i^t = 0 \rightarrow d\left(\overline{U} . \overline{n}\right)_i^t = \left(\frac{\partial u}{\partial x} + \frac{\partial u}{\partial y}\right)_i^t n_{xi}^t + \left(\frac{\partial v}{\partial x} + \frac{\partial v}{\partial y}\right)_i^t n_{yi}^t = 0 \rightarrow \left(\frac{\partial u}{\partial x}\right)_i^t = \frac{\left(\frac{\partial u}{\partial y}\right)_i^t}{\frac{n_{yi}^t - n_{xi}^t}{n_{xi}^t}} + \left(\frac{\partial v}{\partial x}\right)_i^t \quad (8)$$

By solving 4 Eqs. (5 – 8) simultaneously for each sides of the droplet 4 unknown components of **L** are calculated at any time. All four components of velocity gradient tensor are the function of known variables, i.e., normal vector, interfacial tension coefficient, viscosities of droplet and matrix, lateral area of each sector, curvature, and the shear rate of matrix. Eqs (7) and (8) represent L_{yy} as a function of L_{xx}, and L_{xx} as

a function of L_{xy} and L_{yx}, respectively. Thus, L_{xy} and L_{yx} should be determined by Eqs (9) and (14), respectively, and afterward, L_{xx} and L_{yy} would be calculated.

Eq (9) encompasses three terms, namely, the shear rate of matrix, the droplet surface, and the curvature (curvature of three consecutive points) of the droplet, respectively.

$$L_{xyi}^t = (\frac{\partial u}{\partial y})_i^t = \frac{(n_{xi}^t - n_{yi}^t)}{8\mu_d(2n_{xi}^t - n_{yi}^t)}\left(Q_i^t + \Gamma\frac{S_i^t}{V}((n_{yi}^t)^4 - (n_{xi}^t)^4 + 4n_{xi}^t n_{yi}^t) + 4\Gamma\frac{V_i^t}{V}\kappa_i^t((n_{yi}^t)^2 - (n_{xi}^t)^2 + 2n_{xi}^t n_{yi}^t)\right) \quad (9)$$

Equation (14) includes two terms: the shear rate of the matrix including the viscosity difference of two phases, and the velocity gradient L_{xy} including of the normal vector and droplet viscosity.

$$Q_i^t = 2\lambda^{-1}\left|\mu_m - \mu_d\right|\left(\dot{\gamma}_{mxx}\, n_{xi}^t(2n_{yi}^t - n_{xi}^t) + \dot{\gamma}_{mxy}\, n_{yi}^t(2n_{yi}^t - n_{xi}^t) + \dot{\gamma}_{myx}\, n_{xi}^t(2n_{xi}^t + n_{yi}^t) + \dot{\gamma}_{myy}\, n_{yi}^t(2n_{xi}^t + n_{yi}^t)\right) \quad (10)$$

For three consecutive points of (x_{i-1},y_{i-1}),(x_i,y_i), and (x_{i+1},y_{i+1}), the curvature is calculated at each time by Eq (11)[16]. As it is shown in Illustration 1, the volume of each sector (area of the cross-section with the fixed thickness of 1) considering two points on each side and the central point of the droplet, which is the mean of coordinates of all points at the previous time (Eq 13), was calculated by Eq (12)[17].

$$\kappa_i^t = \frac{2\left|\left((x_i^t - x_{i-1}^t)(y_{i+1}^t - y_i^t)\right) - \left((y_i^t - y_{i-1}^t)(x_{i+1}^t - x_i^t)\right)\right|}{\sqrt{\left((x_i^t - x_{i-1}^t)^2 + (y_i^t - y_{i-1}^t)^2\right)\left((x_{i+1}^t - x_i^t)^2 + (y_{i+1}^t - y_i^t)^2\right)\left((x_{i-1}^t - x_{i+1}^t)^2 + (y_{i-1}^t - y_{i+1}^t)^2\right)}} \quad (11)$$

$$V_i^t = \frac{\left|x_i^t(y_{i+1}^t - y_{cent}^t) + x_{i+1}^t(y_{cent}^t - y_i^t) + x_{cent}^t(y_i^t - y_{i+1}^t)\right|}{2} \quad (12)$$

$$x_{cent}^t = \frac{\sum_{i=1}^{1000} x_i^{t-1}}{1000}, y_{cent}^t = \frac{\sum_{i=1}^{1000} y_i^{t-1}}{1000} \quad (13)$$

$$L_{yxi}^t = (\frac{\partial v}{\partial x})_i^t = \frac{\lambda^{-1}\left|\mu_m - \mu_d\right|\left(\dot{\gamma}_{mxx}\, n_{xi}^t n_{yi}^t + \dot{\gamma}_{mxy}\, n_{yi}^t - \dot{\gamma}_{myx}\, n_{xi}^t - \dot{\gamma}_{myy}\, n_{xi}^t n_{yi}^t\right) + \mu_d L_{xyi}^t\left(2(n_{xi}^t - n_{yi}^t)^2 + 8(n_{xi}^t)^2 n_{yi}^t\right)}{2\mu_d\left(-(n_{xi}^t)^2 + 4n_{xi}^t n_{yi}^t + (n_{yi}^t)^2\right)(n_{xi}^t - n_{yi}^t)} \quad (14)$$

$$L_{xxi}^t = \frac{L_{xyi}^t}{\frac{n_{yi}^t - n_{xi}^t}{n_{xi}^t}} + L_{yxi}^t \quad (15)$$

$$L_{yyi}^t = -L_{xxi}^t \quad (16)$$

3- Plotting droplet shape

Knowing the velocity gradient, the lateral areas of the sectors could be calculated by Eq (2), which is equal to the numerical value of the length of the sides. The starting point at any time is assumed to be known, so the coordinates of second point would be calculated by solving Eqs (17) and (18). The coordinates of other points would be determined this way, one after another. These plotted points would be the initial shape of the next time. Normal vectors are perpendicular to the surface; therefore, by 90 degree rotation, the tangential vectors (**T**) would be calculated. That means when knowing the first rotated normal vector, the second point would be calculated, and by knowing the second rotated normal vector, the third point would be obtained; this will continue to 999th rotated normal vector. Fig. 4 shows the flowchart of calculating droplet surface points until the break-up time.

$$\sqrt{(x_{i+1}^t - x_i^t)^2 + (y_{i+1}^t - y_i^t)^2} = \left|S_i^t\right| \tag{17}$$

$$y_{i+1}^t - y_i^t = m_i^{t-1}\left(x_{i+1}^t - x_i^t\right) \tag{18}$$

$$\begin{bmatrix} T_x \\ T_y \end{bmatrix} = \begin{bmatrix} \cos\theta & -\sin\theta \\ \sin\theta & \cos\theta \end{bmatrix} \begin{bmatrix} n_x \\ n_y \end{bmatrix} \tag{19}$$

$$m_i^{t-1} = \left(\frac{T_y}{T_x}\right)_i^{t-1} \tag{20}$$

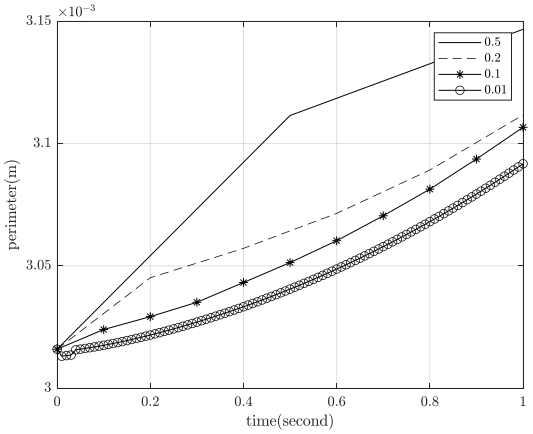

Fig. 2. Changing the lateral area of the drop according to the time step from 0.5 to 0.01

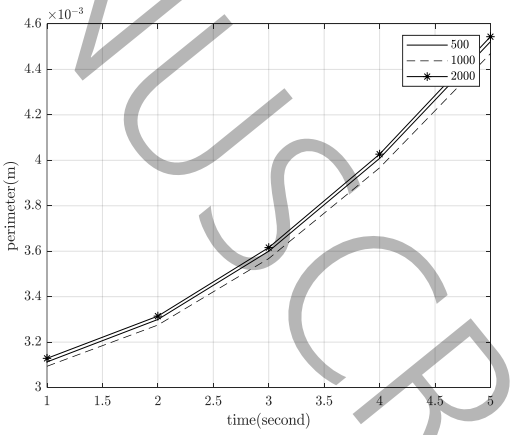

Fig. 3. Changing the lateral area of the drop according to the number of sides of the drop from 500 to 2000

As can be seen, Eqs (1) and (2) are solved using the forward Euler method. Therefore, it is necessary to determine the convergence interval of the time step (Δt). The convergence interval of time step is between

0.5 - 0.01. To determine the optimal time step, the equations are solved with 4 different time steps and the results are presented in Fig 2. As can be seen, the time steps of 0.01 and 0.1 have very small difference. Therefore, the optimal time step (in terms of accuracy and speed of solution) is considered to be 0.1. In the same way, the optimal number of sides is 1000 sides due to the very small difference between all three numbers (500, 1000 and 2000). The convergence interval of number of drop sides is between 500-2000. Theoretically, there is no limit to the droplet size in this method. The shear rate of the matrix may be either lower or higher than the rate required to break up the droplet. The ratio of droplet viscosity to matrix can be less or greater than 1.

Fig. 4. Flowchart to plot the shape of droplet

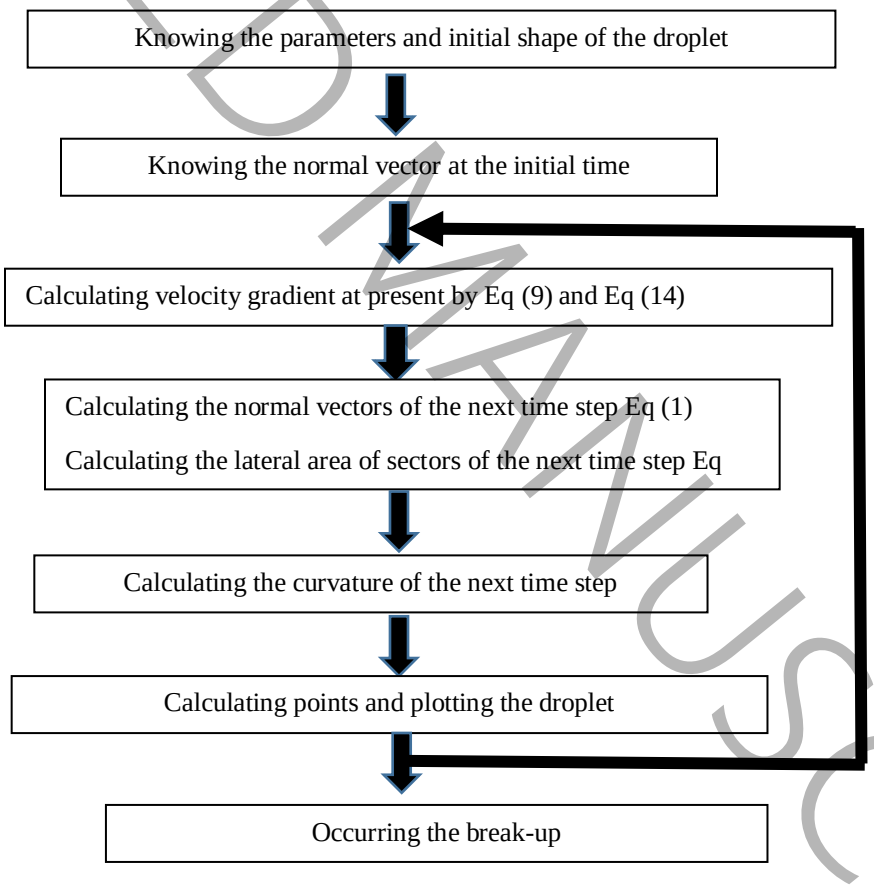

4- Results

Fig. 4 shows four series of parameters for calculating velocity gradients and coordinates of points used from the previous study; Figs 25 and 26 depict the experimental results of droplet deformation[18, 19]. Each series with different Reynolds and Capillary numbers were used to compare the results of the simulation of

the model versus experimental results more precisely. Figs 5, 10, 15, and 20, show the droplet shape deformation during the time until the break-up for all four series respectively.

A new parameter is recommended to predict the break-up time more accurately. The parameter is called the shape factor and is obtained by Eq. (21), which expresses the maximum change of the slope ratio of every side of the droplet at present to the previous time.

Figs. 6, 11, 16, and 21 display the shape factor parameter at every time for four series, respectively; the peak of each figure also indicates the time at which the droplet has deformed into a thread containing the ends bulb. In other words, at the time when the shape factor has got a maximum number, the changing of the slope of sides between the thread and bulb will change the most. Figs. 7, 12, 17, and 22 specify the ratio of the elongated shape of the droplet to the initial radius that increases continuously. This increase has grown over time because of decreasing thread diameter and the consequent decrease in the resistance of droplets. Concerning Fig. 27, the results of thread diameter (criteria of elongation droplet) by the simulated and experimental methods for series 1 are in line with less than a five percent deviation. In series 2,3, and 4, the viscosity of the droplet and viscosity of the matrix was lower than in series 1, which made the ratio of shape relaxation to shear force greater and the deviation greater than that of series 1. By comparing series 2,3 and 4, it is clear that when the Capillary number got near the critical Capillary number (1.1Cac), the force of shape relaxation became more effective. As shown, the deviation is more significant. As could be predicted, by increasing the Capillary number to 1.98 and then 2.6, the simulation and experimental results of the thread diameter became less deviated. One of the most important terms that changes by the deformation of the droplet are the rate of the lateral area of the droplet over time. Then, as it is evident in Fgs 8, 13, 18, and 23, the slope of the lateral area change grows gradually until the break-up. Likewise, these Illustrations show that the dominant mechanism of droplet deformation of series 1-3 is elongating end pinching. This mechanism means shear flow force overcomes interfacial tension, and the droplet length increases until the break-up. In other words, it means that the lateral area of the droplet would constantly increase at each time, even after the formation of the dumbbell, then the formation of the bulb, until it breaks up (These times are the peaks of Figs. 6, 11, 16, 21 respectively). Therefore as it is clarified in Fig

28, the value of bulb diameter for simulated results of series 1-3 is greater than that of the experimental results, whereas, for series 4, this value for the experimental result is greater than that of the simulated result. This confirms that for series 1-3 shape relaxation term is negligible, but for a lower Capillary number, the contribution of shape relaxation becomes more effective.

$$SF_t = Maximum(\frac{m_i^t}{m_i^{t-1}}) \qquad (21)$$

In Figs 9, 14, 19, and 24, changes in the velocity gradients at any points of the droplet by the scale of $-\pi$ to π radian (the starting point for drawing the shape is at $-\pi$ radian) are remarked at the time of the break-up, respectively. As expected, L_{xx} and L_{yy} have lower values than L_{xy} and L_{yx}. Also, as can be seen in these graphs, there are four plateau regions of the velocity gradient, which indicate the presence of two bulbs.

The velocity gradient tensor is assumed to be constant along each side, so knowing **L** at each side (point) of the droplet, the velocities (u, v) could be calculated.

Table 1 – 4 series of parameters used for simulation

	μ_m(Pa.s)	μ_d(Pa.s)	Γ(mN/m)	$\dot{\gamma}$ (s^{-1})	r_0(mm)	Ca	Re
Series 1	7	4.3	10.7	2.17	0.48	$1.40Ca_c$	<0.01
Series 2	0.86	0.43	4.3	9	0.42	$1.98Ca_c$	>0.2
Series 3	0.86	0.43	4.3	5.2	0.95	$2.60Ca_c$	>0.3
Series 4	0.86	0.43	4.3	3.8	0.55	$1.10Ca_c$	>0.1

One important reason for using the velocity gradient on the drop instead of the shear rate is that the velocity gradient is not a symmetric tensor. This means that the term related to solid body rotation, along with the pure elongation term, is present in the velocity gradient tensor. As a result, both the physical phenomena of rotation and drop stretching can be observed in the slope of the model. This eliminates the need to calculate the rotation phenomenon separately.

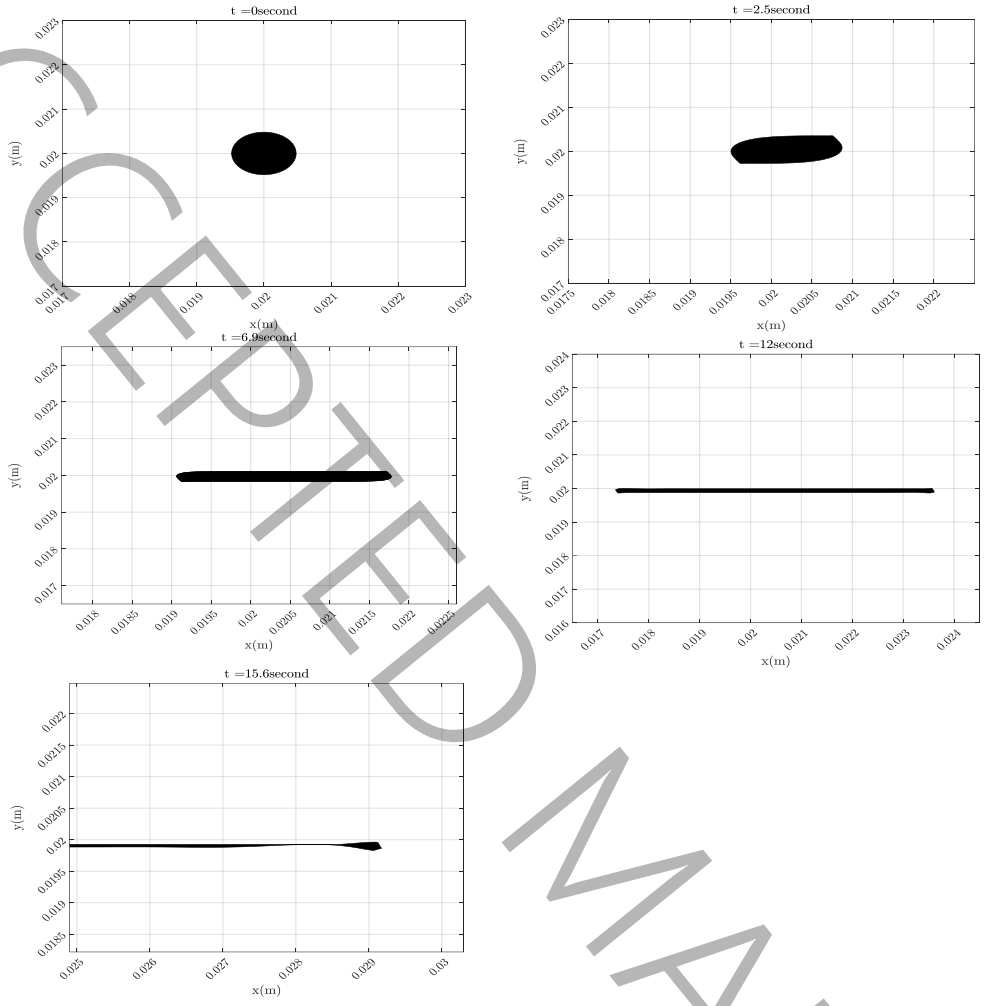

Fig. 5. Simulation of deformation of viscous droplet under the shear flow of viscous matrix from zero to 16th second (series 1).

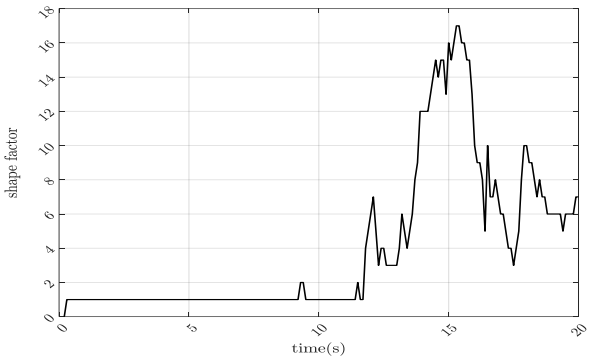

Fig. 6. Change of the shape factor vs time (series 1)

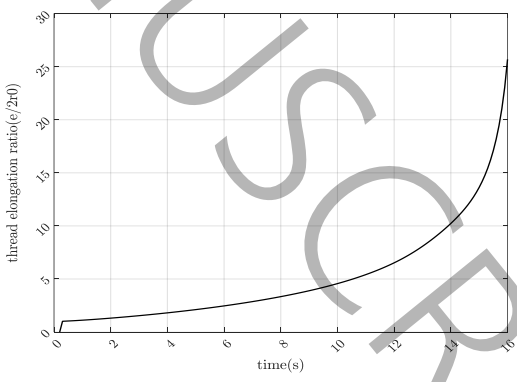

Fig. 7. Thread elongation ratio from zero to 16th second (series 1).

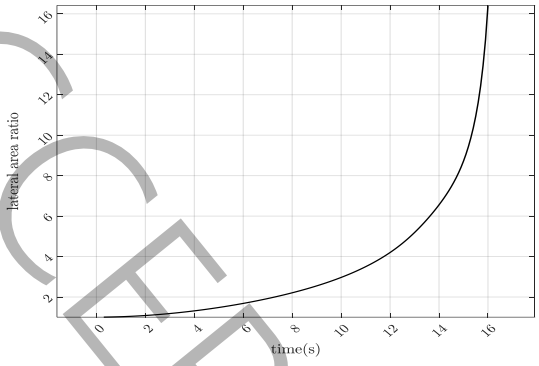

Fig. 8. Change of the lateral area of droplet from zero to 16th second (series 1).

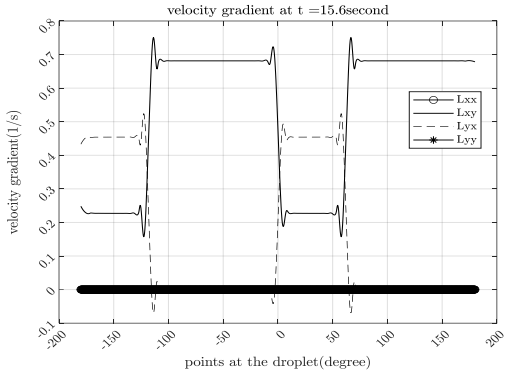

Fig. 9. Velocity gradient of each point of the droplet at 15.6 second (series 1).

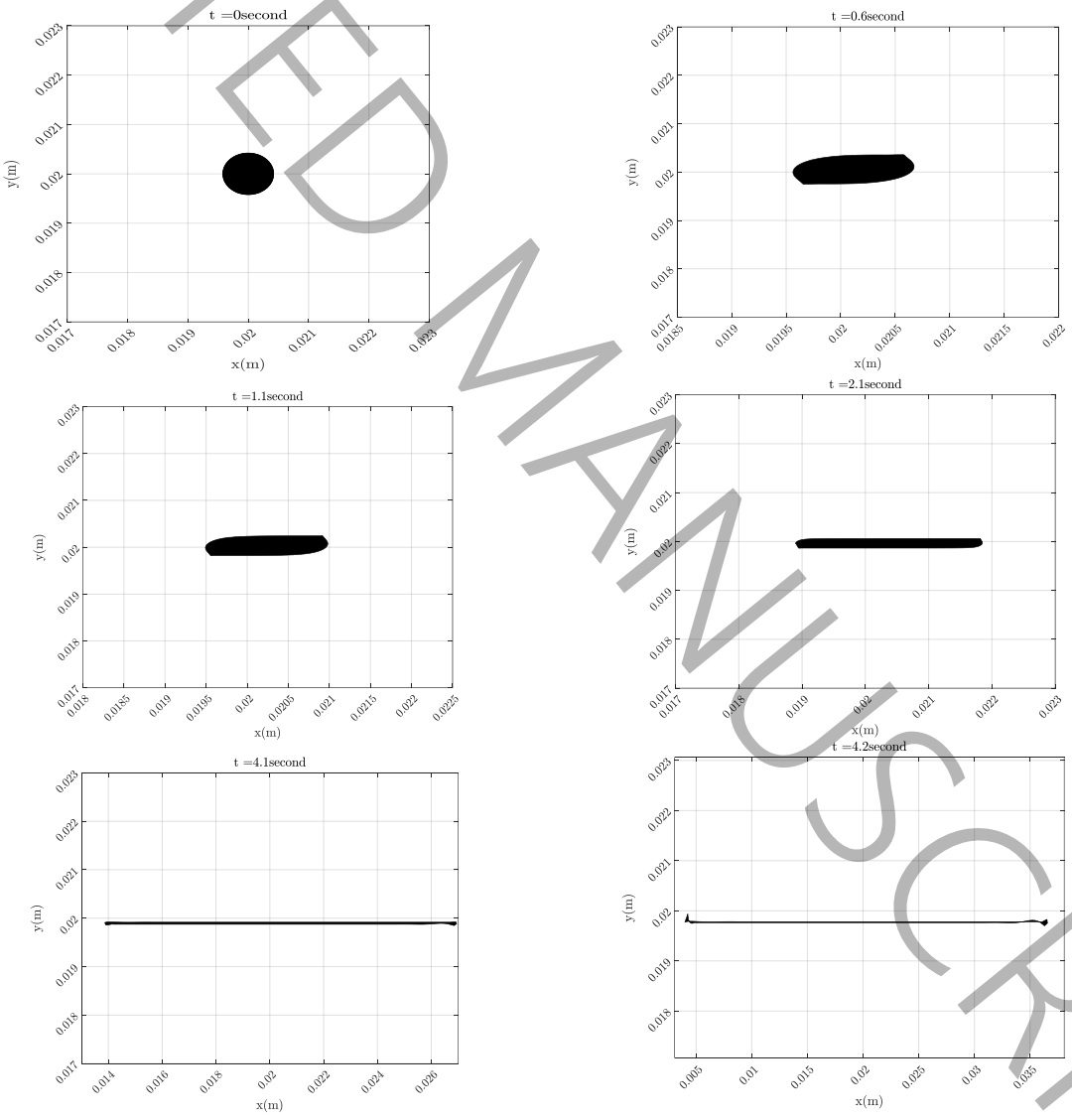

Fig. 10. - Simulation of deformation of viscous droplet under the shear flow of viscous matrix from zero to 5th second (series 2).

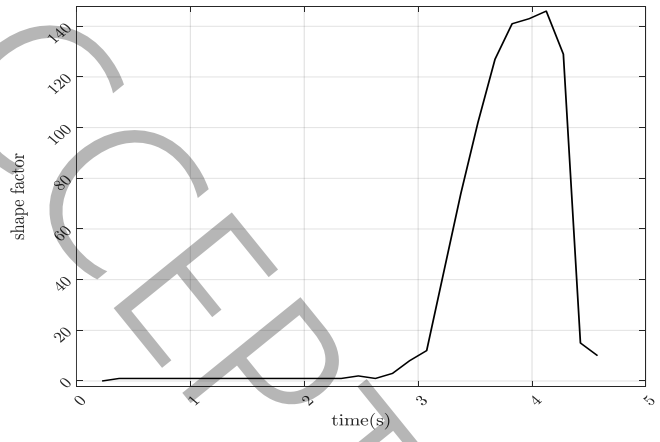

Fig. 11. Changes of the shape factor vs time (series 2).

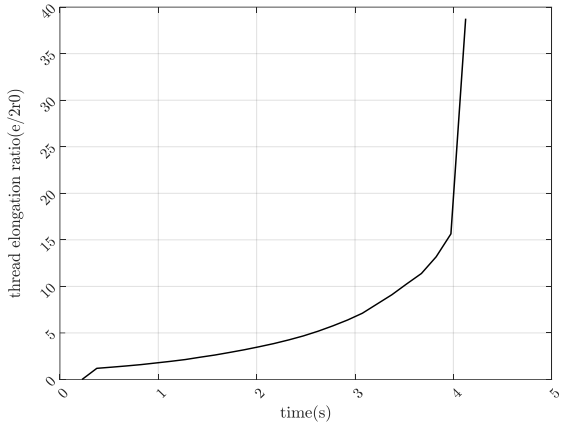

Fig. 12. Thread elongation ratio from zero to 5th second (series 2).

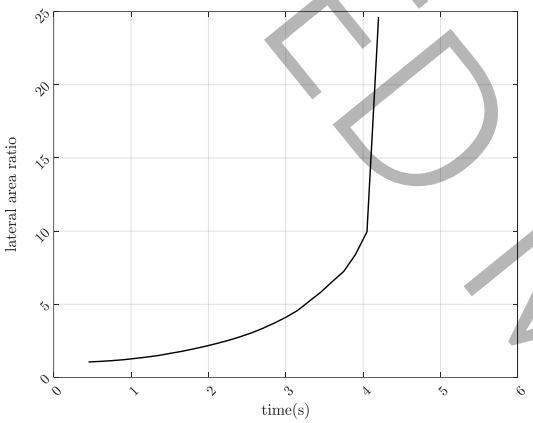

Fig. 13. Changes of the lateral area of the droplet from zero to 5^{h} second (series2).

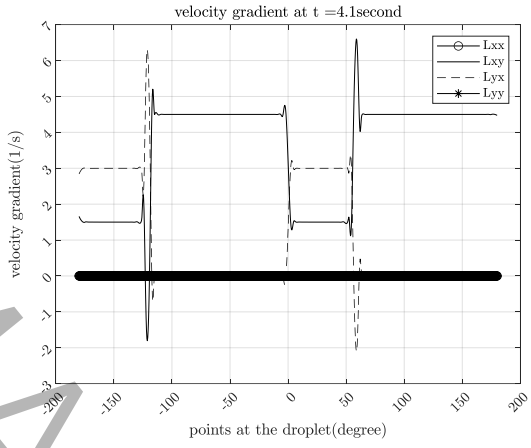

Fig. 14. Velocity gradient of each point of the droplet at 4.1 second (series 2).

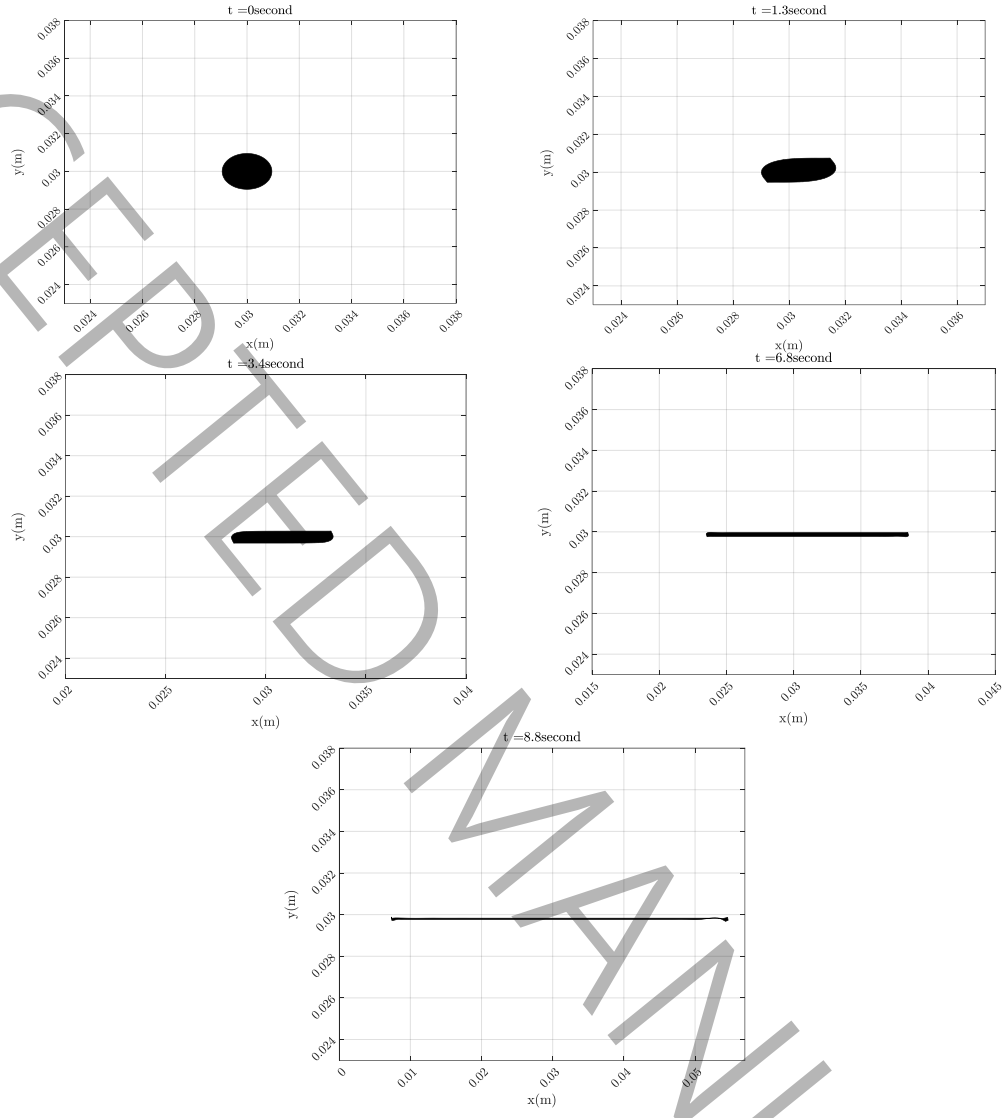

Fig. 15. Simulation of deformation of viscous droplet under the shear flow of viscous matrix from zero to 9th second (series 3).

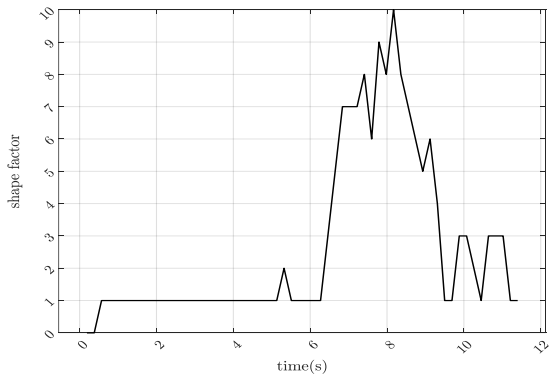

Fig. 16. Changes of the shape factor vs time (series 3).

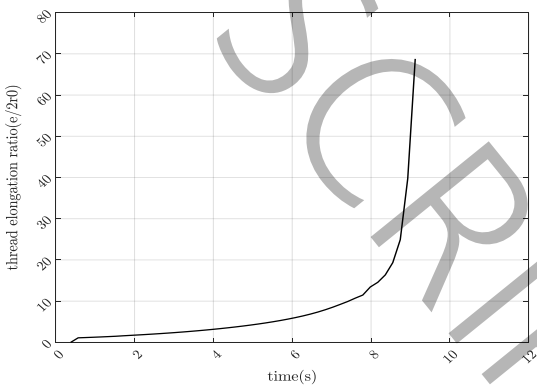

Fig. 17. Thread elongation ratio from zero to 9th second (series 3).

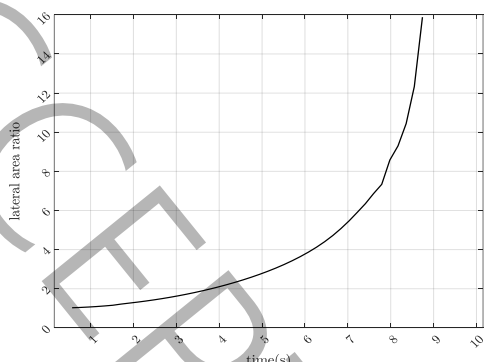

Fig. 18. Changes of the lateral area of droplet from zero to 9th second (series 3).

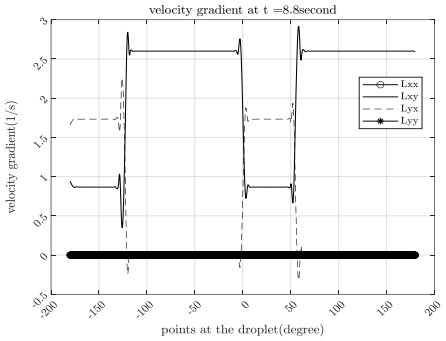

Fig. 19. Velocity gradient of each point of the droplet at 8.8 second (series 3).

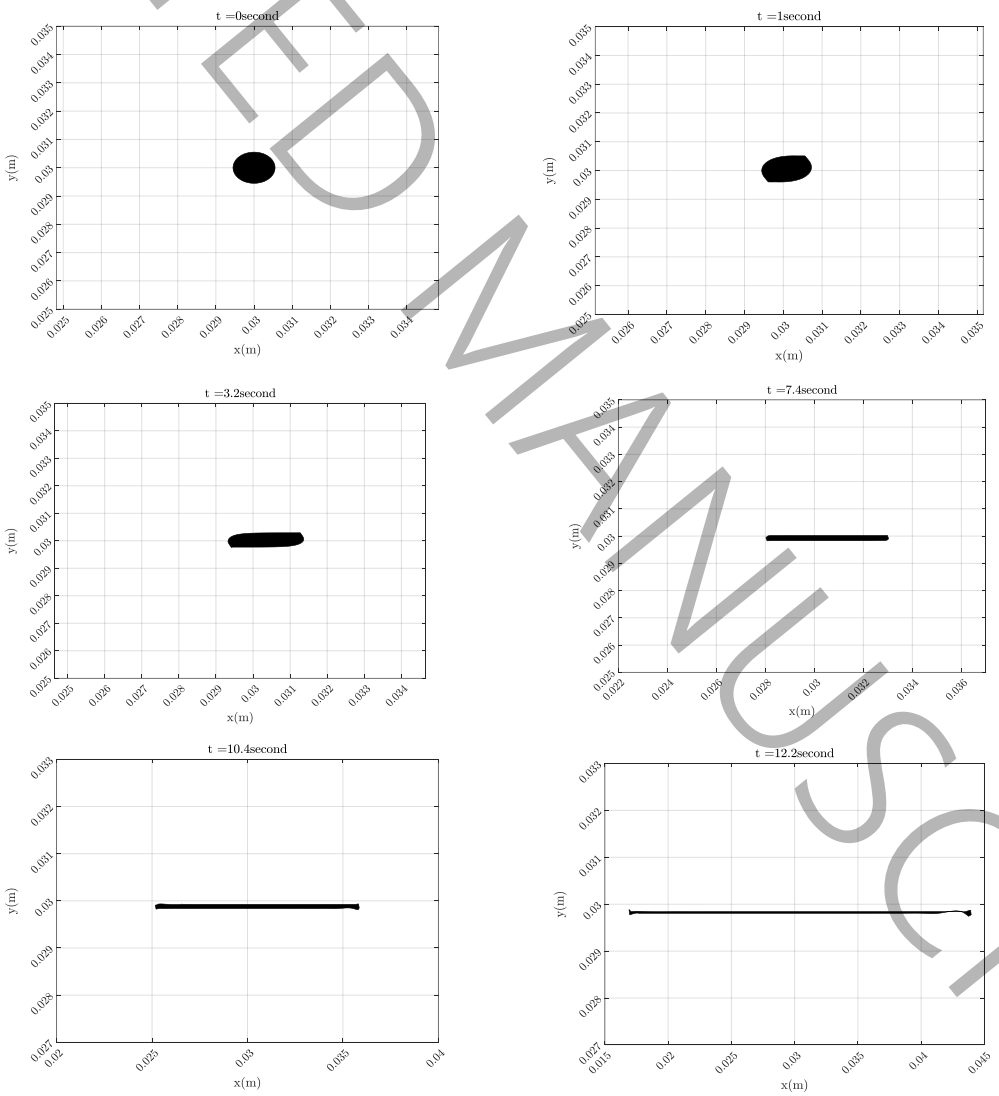

Fig. 20. Simulation of deformation of viscous droplet under the shear flow of viscous matrix from zero to 13th second (series 4).

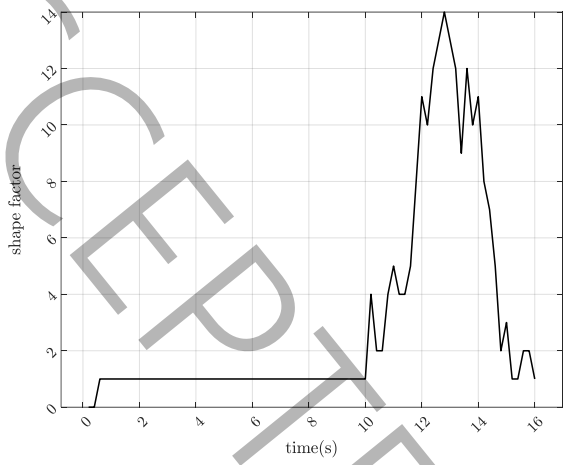

Fig. 21. Changes of the shape factor vs time (series 4).

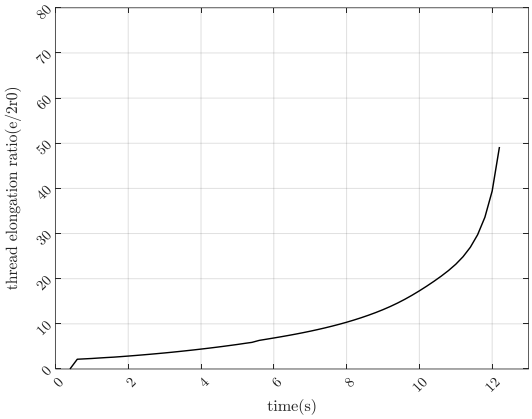

Fig. 22. Thread elongation ratio from zero to 13th second (series 4).

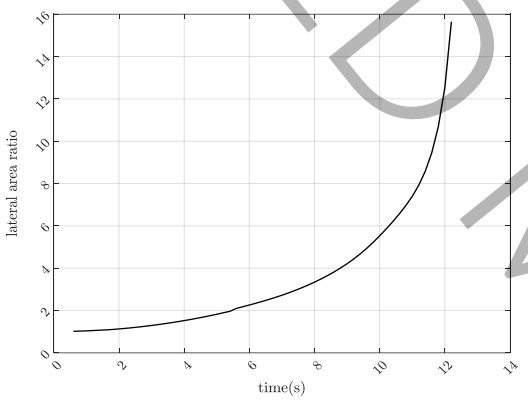

Fig. 23. Changes of the lateral area of droplet from zero to 13th second (series 4).

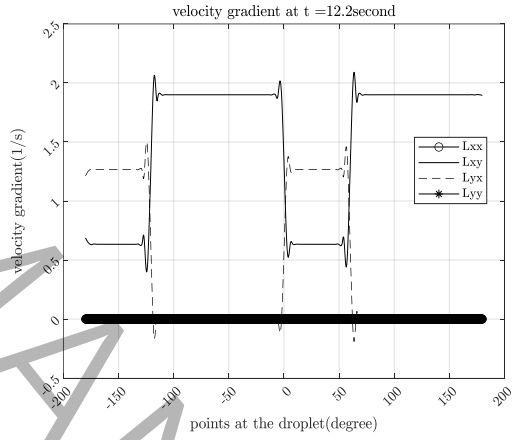

Fig. 24. Velocity gradient of each point of the droplet at 12.2 second (series 4).

5- Conclusion

The proposed model for predicting droplet deformation and break-up is based on the deformation of normal vectors of the lateral surface of the droplet. Thus, solving the Equations at the interface of droplet and matrix instead of solving the equations over the total volume of matrix and droplet has made the proposed model faster than other control volume methods. On the other side, this model is independent of the initial shape of the droplet. One of the most important applications of this model is calculating the velocity profile over and around the droplet at each time by knowing the velocity gradient without needing the solution of velocity equations such as Navier-Stokes equations.

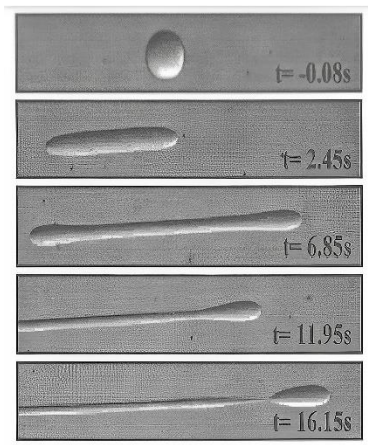

Fig. 25. Experimental result of deformation of the droplet under shear in the matrix (series 1) Reproduced with the permission of Marks.[18]

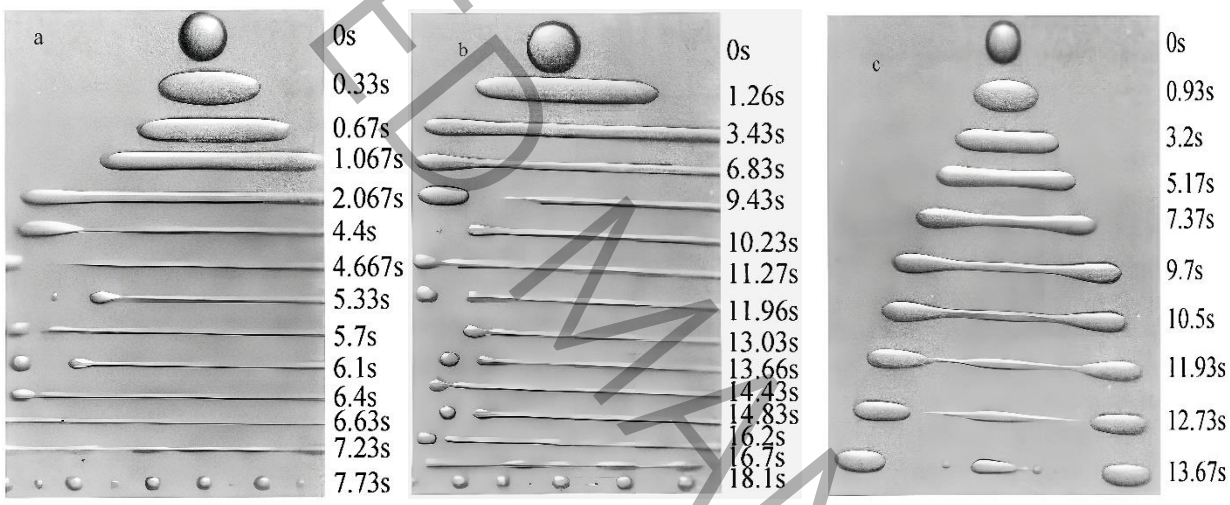

Fig. 26. (a) Experimental result of deformation of the droplet under shear in the matrix (series 2). (b) Experimental result of deformation of the droplet under shear in the matrix (series 3).). (c) Experimental result of deformation of the droplet under shear in the matrix (series 4).Reproduced with permission from Chin. J. Chem. Eng ,15 (1), (2007). Copyright 2007 Elsevier.[19]

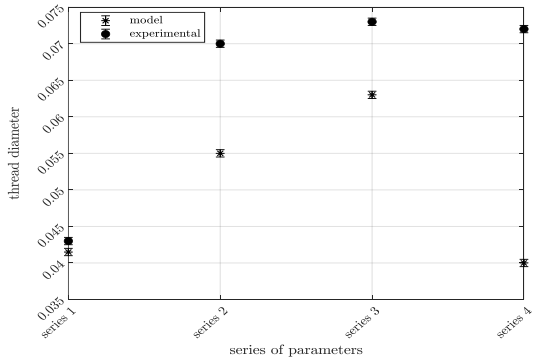

Fig. 27. Comparing the thread diameters predicted by model vs experimental results at break-up.

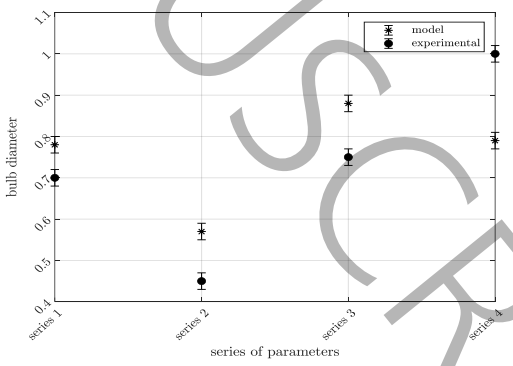

Fig. 28. Comparing the bulb diameters predicted by model vs experimental results at break-up.

By comparing Figs. 6, 11, 16, and 21 (shape factor parameter) with Figs. 25- 26 (experimental results of the

droplet break-up), it is clear that the time of break-up for four series of simulation and experimental results are in line with the second accuracy. However, as is clarified in Table 2(summary of Figs 27, 28), at a lower Reynolds number (series 1), the thread diameter calculated by the model coincides accurately with the experimental results. Table 3 shows, the simulation and experimental results of the stretched droplet Length/Diameter ratio and the Bulb/Thread volume ratio are compared. Near the critical capillary number, due to the change of the failure mechanism from end pinching to middle pinching, the final bubble/droplet volume ratio and the droplet length/diameter ratio in the simulation show a greater deviation from the experimental results (series 4). By growing the Reynolds number at the lower Capillary number and viscosity of the matrix (series 4), the radius of the thread and the bulb size at the break-up time display more deviation. This deviation is because the proportion of shape relaxation force is increased while shear force is decreased by decreasing viscosities.

The dominant mechanism for this Capillary range near the critical is the necking mechanism. It means that from initial times the droplet shape becomes dumbbell-like (not thread), and at the time of break-up, two new droplets with equal size are gained.

Therefore, by increasing the Capillary number, the shapes coincide more accurately. The results of series 1 were more consistent with experimental data than those of series 2 and 3 because of the more significant proportion of shear flow force. This is because the higher Capillary number responds better by growing the Reynolds number.

Finally, the presented model for plotting and calculating the break-up of viscous droplets in a viscous matrix is helpful for the middle range of the Capillary number (1.40 Ca_c-2.60 Ca_c) and the lower range of the Reynolds number .Our analysis shows that the drop's dimensions deviate by less than 30% and its rotation by less than 20% when compared to experimental results. Moreover, the end bubble's dimension shows a deviation of less than 40%. These findings demonstrate the high level of accuracy and consistency of our methodology, making it a valuable tool for future research and experimentation. The dominant mechanism

predicted by this model is the elongating end pinching break-up. The advantage of this model compared to previous methods is the faster calculation speed due to equation checking on the interface.

It is suggested to implement the presented model in three dimensions and study different materials for the experimental section in future research.

Table 2 – Comparison of simulated droplet dimensions and experimental results at break-up

	Thread Diameter (model)mm	Thread Diameter (experimental)mm	Bulb Length (model)mm	Bulb Length (experimental)mm	d_0(mm)	*Ca*	*Re*
Series 1	0.0415	0.0430	0.7800	0.7000	0.96	$1.40Ca_c$	<0.01
Series 2	0.0550	0.0700	0.5700	0.4500	0.84	$1.98Ca_c$	>0.2
Series 3	0.0630	0.0730	0.8800	0.7500	1.9	$2.60Ca_c$	>0.3
Series 4	0.0400	0.0720	0.7900	1.0000	1.1	$1.10Ca_c$	>0.1

Table 3 –Comparison the parameters of Length/Diameter and Bulb/Thread volume of simulated droplet and experimental results at break-up

	Thread Length/Diameter(model)	Thread Length/Diameter (experimental)	Bulb Length/Diameter (model)	Bulb Length/Diameter (experimental)	Bulb/Thread volume ratio (model)	Bulb/Thread volume ratio (experimental)
Series 1	409	389	2.7	2.85	0.073	0.081
Series 2	618	482	4.1	3.8	0.058	0.071
Series 3	825	643	3.4	2.9	0.055	0.083
Series 4	675	250	4.8	3.2	0.07	0.16

Nomenclature :

e : length of thread at every time

Ca : Capillary number ($Ca = \frac{r_0 \mu_m \dot{\gamma}_m}{\Gamma}$)

d_0 : initial diameter of the droplet

L: velocity gradient tensor at the droplet interface

m : the slope of each side of the droplet at time t

n : the normal vector of each point at the droplet interface

Q : shear rate term of xy component of the calculated velocity gradient (L_{xy})

r_0 : initial radius of the droplet

S : lateral area of each side of the droplet

T : the tangential vector of each point at the droplet interface

V_i : the volume of every sector of the droplet

u : x-direction velocity at the interface of the droplet

v : y-direction velocity at the interface of the droplet

$\bar{U} = (u, v)$

Superscript

t : time

Subscript:

i : the points of the droplet

(x_{cent}^t, y_{cent}^t) : the coordinate of the center point of the droplet at time t

Greek symbols:

Δt : time step

$\dot{\boldsymbol{\gamma}}_{\mathbf{m}} = \begin{bmatrix} 0 & \dot{\gamma}_{mxy} \\ \dot{\gamma}_{myx} & 0 \end{bmatrix}$: shear rate tensor of matrix

μ_d : the viscosity of the droplet

μ_m : the viscosity of the matrix

$\lambda = \frac{\mu_d}{\mu_m}$

Γ : the interfacial tension coefficient

κ : the curvature at the interface of the droplet (the curvature of three consecutive points)

$\boldsymbol{\sigma_{over}}$: stress tensor over the interface

$\boldsymbol{\sigma_{d}}$: stress tensor inside the interface

$\boldsymbol{\sigma_{TANGENTIAL}}$: tangential stress balance at the interface

$\boldsymbol{\sigma_{NORMAL}}$: normal stress balance at the interface

References:

[1] W. Schowalter, C. Chaffey, H. Brenner, Rheological behavior of a dilute emulsion, Journal of colloid and interface science, 26(2) (1968) 152-160.

[2] J. Mellema, M. Willemse, Effective viscosity of dispersions approached by a statistical continuum method, Physica A: Statistical Mechanics and its Applications, 122(1-2) (1983) 286-312.

[3] M. Doi, T. Ohta, Dynamics and rheology of complex interfaces. I, The Journal of chemical physics, 95(2) (1991) 1242-1248.

[4] H.M. Lee, O.O. Park, Rheology and dynamics of immiscible polymer blends, Journal of Rheology, 38(5) (1994) 1405-1425.

[5] J. Rallison, The deformation of small viscous drops and bubbles in shear flows, Annual review of fluid mechanics, 16(1) (1984) 45-66.

[6] I. Vinckier, M. Minale, J. Mewis, P. Moldenaers, Rheology of semi-dilute emulsions: viscoelastic effects caused by the interfacial tension, Colloids and Surfaces A: Physicochemical and Engineering Aspects, 150(1-3) (1999) 217-228.

[7] R. Pal, Rheology of simple and multiple emulsions, Current opinion in colloid & interface science, 16(1) (2011) 41-60.

[8] N. Singh, V. Narsimhan, Deformation and burst of a liquid droplet with viscous surface moduli in a linear flow field, Physical Review Fluids, 5(6) (2020) 063601.

[9] A. Håkansson, L. Brandt, Deformation and initial breakup morphology of viscous emulsion drops in isotropic homogeneous turbulence with relevance for emulsification devices, Chemical Engineering Science, 253 (2022) 117599.

[10] S. Sahu, A.S. Khair, Dynamics of a viscous drop under an oscillatory uniaxial extensional Stokes flow, International Journal of Multiphase Flow, 146 (2022) 103844.

[11] J. Li, Y. Renardy, Numerical study of flows of two immiscible liquids at low Reynolds number, SIAM review, 42(3) (2000) 417-439.

[12] B. Jalili, P. Jalili, Numerical analysis of airflow turbulence intensity effect on liquid jet trajectory and breakup in two-phase cross flow, Alexandria Engineering Journal, 68 (2023) 577-585.

[13] S. Heydarpoor, N.M. Famili, Polygon model for solution of non-linear velocity gradient of interface and asymmetric break-up of droplet, Physics of Fluids, 36(1) (2024).

[14] R. Abeyartne, Continuum Mechanics Volume II of Lecture Notes on The Mechanics of Elastic Solids Cambridge, http, web. mit. edu/abeyartne/lecture_notes. html, 11 (2012).

[15] L.G. Leal, Advanced transport phenomena: fluid mechanics and convective transport processes, Cambridge University Press, 2007.

[16] J.-C. Léger, Menger curvature and rectifiability, Annals of mathematics, 149(3) (1999) 831-869.

[17] V. Ivanoff, C. Pinzka, J. Lipman, E1376, The American Mathematical Monthly, 67(3) (1960) 291-292.
[18] C.R. Marks, Drop breakup and deformation in sudden onset strong flows, University of Maryland, College Park, 1998.
[19] L. Changzhi, G. Liejin, Experimental study of drop deformation and breakup in simple shear flows, Chinese Journal of Chemical Engineering, 15(1) (2007) 1-5.